PHYSICAL REVIEW LETTERS

Published week ending 22 SEPTEMBER 2023

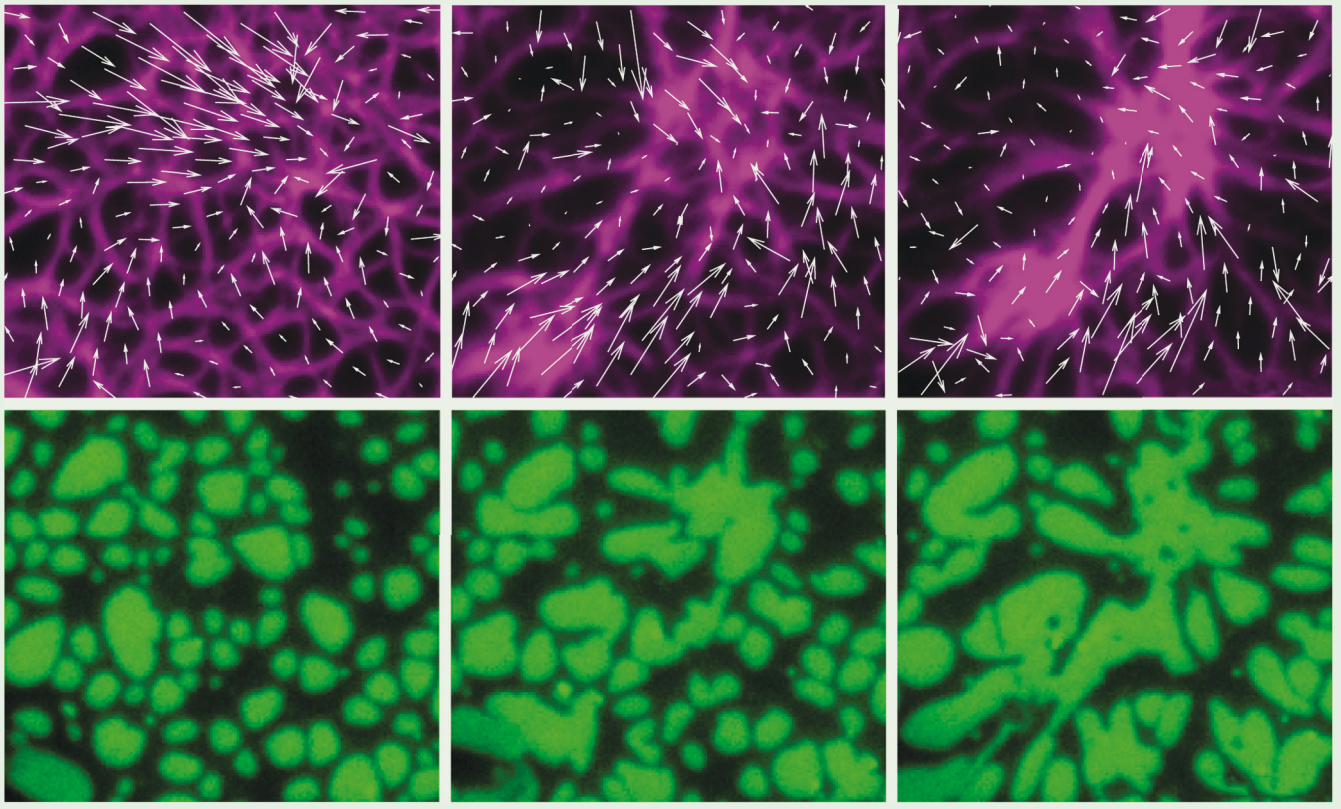

Published by
American Physical Society

APS

Volume 131, Number 12

Active Surface Flows Accelerate the Coarsening of Lipid Membrane Domains

Daniel P. Arnold,* Aakanksha Gubbala,* and Sho C. Takatori†
Department of Chemical Engineering, University of California, Santa Barbara, Santa Barbara, California 93106, USA

(Received 31 May 2023; accepted 24 August 2023; published 21 September 2023)

Phase separation of multicomponent lipid membranes is characterized by the nucleation and coarsening of circular membrane domains that grow slowly in time as $\sim t^{1/3}$, following classical theories of coalescence and Ostwald ripening. In this Letter, we study the coarsening kinetics of phase-separating lipid membranes subjected to nonequilibrium forces and flows transmitted by motor-driven gliding actin filaments. We experimentally observe that the activity-induced surface flows trigger rapid coarsening of noncircular membrane domains that grow as $\sim t^{2/3}$, a 2x acceleration in the growth exponent compared to passive coalescence and Ostwald ripening. We analyze these results by developing analytical theories based on the Smoluchowski coagulation model and the phase field model to predict the domain growth in the presence of active flows. Our Letter demonstrates that active matter forces may be used to control the growth and morphology of membrane domains driven out of equilibrium.

DOI: 10.1103/PhysRevLett.131.128402

The dynamic interplay between nonequilibrium forces and membrane surfaces plays an essential role in many physical processes in living systems. For example, molecular motors and the cytoskeleton inside living cells generate active forces on the cell membrane, allowing cells to bend, flow, and stretch the cell surface [1,2]. Reconstituted multicomponent lipid membranes can also phase separate into macroscopic domains along the membrane [3]. While the nucleation and coarsening kinetics of lipid membrane domains at thermodynamic equilibrium is well established [4–8], we have little understanding of how membrane domains grow when subjected to nonequilibrium forces and flows, such as those that might be generated by the actin cytoskeleton.

In this Letter, we experimentally and theoretically study the effect of internally driven 2D active flows on the rate of domain coarsening in phase-separated lipid bilayers. In the absence of active flows [Fig. 1(a), Supplemental Material [9], Video S1], the lipids form circular mesoscopic domains that grow slowly with time, consistent with prior work on giant vesicles [7]. We find that actin and myosin create internally driven surface flows, which couple with domains [Fig. 1(b)] and drive coarsening and growth according to much faster dynamics than passive systems. In passive systems, the scaling exponent of $\alpha = 1/3$ is well established for domains of size a that grow with time t according to $a \sim t^{\alpha}$, for both coalescence and Ostwald ripening mechanisms [4,5,7,10,11].

Previously, it has been shown that linear, externally imposed flows can deform domains and accelerate coarsening [12–14]. Here we describe a system in which surface-adsorbed active matter, in the form of an actomyosin cortex, internally drives lipid flows, which lead to rapid domain growth. Using Cahn-Hilliard simulations, we show that the

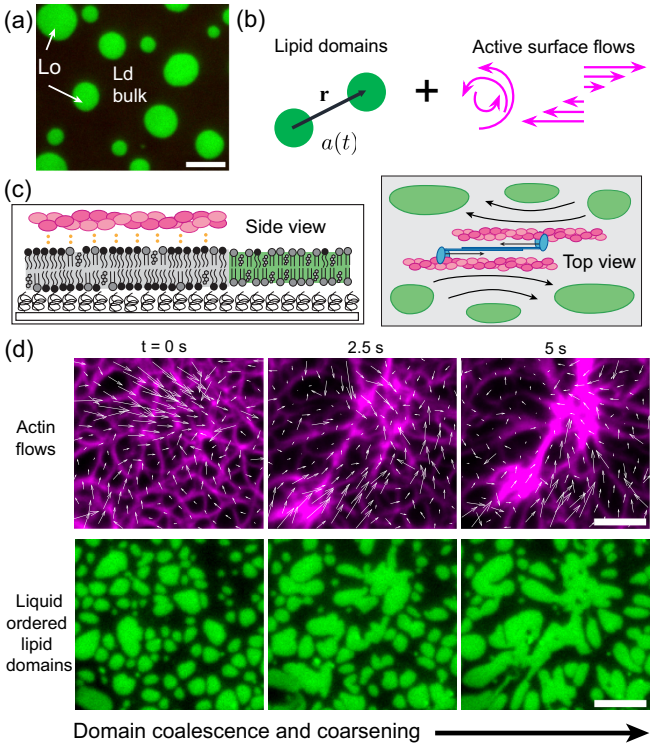

FIG. 1. (a) Planar lipid bilayers phase-separate into Lo and liquid-disordered Ld phases. (b) In this Letter, we study the growth of lipid domains of size a under 2D flows generated by internal "active" forcing. (c) Left: in our experiments, actin is bound to the Ld phase, avoiding the Lo phase. Right: actomyosin contraction internally drives lipid membrane flows. (d) Time-lapse images of actin (magenta) contraction with vectors calculated from particle image velocimetry overlaid (top), and Lo lipid domains growing in time (green, bottom). Scale bar is 5 μm.

in-plane flows created by actin increase α by more than a factor of 2 at moderate Péclet numbers of 10^{-3}–10^{-2}. We compare these results to analytical theory and simulations describing domain growth under simple shear flow, finding that the behavior of flow-based mechanisms is consistent with the experimental results for actin-driven coarsening.

Experiments.—A planar lipid bilayer is deposited on a cushioned glass coverslip, treated with polymer and proteins to prevent kinetic arrest of domains due to friction with rough substrates (see Supplemental Material for detailed methods [9]). Briefly, silica coverslips are treated with chlorotrimethylsilane before heavy meromyosin and polylysine-grafted polyethylene glycol are adsorbed to the surface. Giant unilamellar vesicles (GUVs) are formed at 50 °C with 45% dioleoylphosphatidylcholine, 35% dipalmitoylphosphatidylcholine, 15% cholesterol, and 5% dioleoyl-3-trimethylammonium propane (DOTAP) using established electroformation methods [15] and then allowed to rupture on the treated coverslip, creating a planar bilayer. At room temperature, this lipid composition phase separates into a continuous liquid-disordered (Ld) phase containing dispersed liquid-ordered (Lo) domains [Fig. 1(a)] [3]. Small amounts of lipid dyes are added to each phase for fluorescence imaging [16].

Bilayers are heated to 37 °C and decorated with filamentous actin (F-actin) [17], a negatively charged cytoskeletal protein, which adsorbs to the bilayer via electrostatic attraction to positively charged DOTAP enriched in the Ld phase [Fig. 1(c), left] [18]. Myosin II motor proteins [19,20] are added in a rigor (ATP-free) state, causing them to cross-link actin but not apply any contractile force [Fig. 1(c), right]. Upon quenching the system to room temperature, the Lo domains reform and actin is sequestered into the Ld phase [Figs. 1(c) and 1(d)]. Unlike the circular domains in Fig. 1(a), the domains in Fig. 1(d) initially adopt a morphology characterized by sharp corners and elongated edges, as they have low line tension and are forced to conform to actin bundles [21,22]. These actin-constrained domains reach a steady size and do not appreciably grow over tens of minutes.

Upon introducing ATP, we observe rapid actomyosin contraction, along with simultaneous elongation and growth of lipid domains [Fig. 1(d), Supplemental Material [9], Video S2]. The most dramatic contraction is often very short-lived (< 5 s) as the actin forms contractile clusters and generates surface flows that rapidly coarsen the Lo domains. Figure 1(d) (top) shows the actin flow field generated by particle image velocimetry (PIV) and confirms that in-plane actin flows are directed toward an apparent sink in the upper right quadrant of the image.

We threshold time-lapse images of the domains and track the area-to-perimeter ratio of the resulting binary images as a metric for characteristic domain size $a(t)$, consistent with prior experimental work on lipid domain growth [7]. This definition of the characteristic domain size is consistent

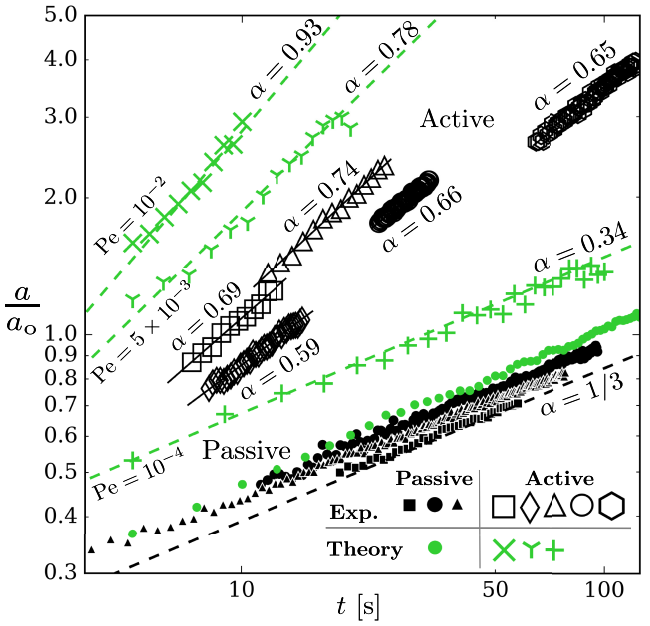

FIG. 2. Lo lipid domain size $a(t)$ is plotted as a function of time t for experiments (black) and Cahn-Hilliard numerical calculations (green), with growth exponents α presented for each: $a \sim t^{\alpha}$. Closed symbols represent passive domain growth in the absence of flow, with circles and triangles representing three independent passive experiments. Passive domains grow as $\alpha = 1/3$ (dashed black line), consistent with classical theories on coalescence and Ostwald ripening. Open symbols represent active domain growth in the presence of 2D flow, either imposed experimentally via actomyosin contraction or incorporated theoretically using particle image velocimetry from experiments [Fig. 1(d)]. Five independent active experiments are presented, along with simulations using three different Péclet numbers (Pe). Each dataset is rescaled by a different factor a_0 to capture the power law scaling exponents.

with the alternative definition based on the first moment of the static structure factor, $a(t) \sim (\int kS(k,t)dk / \int S(k,t)dk)^{-1}$, where k is the wave vector (see Supplemental Material [9]). We fit the resulting data to the equation $a(t) = (At + B)^{\alpha}$ before rescaling the time to give the form $a \sim t^{\alpha}$ (see Supplemental Material). Figure 2 shows the growth of $a(t)$ over time for five independent experiments with actomyosin activity (black open symbols). We find growth exponents range from $\alpha = 0.59$ to 0.74 for these domains under internally driven, active surface flows.

We measure the active coarsening rate across five different membrane compositions and actin densities, without observing a strong correlation between coarsening rate and composition (Supplemental Material [9], Fig. S1) or actin density (Fig. S2 [9]) over the range tested. We perform an additional control experiment in which we quench the bilayer and add ATP simultaneously; we observe the passive scaling of $\alpha = 1/3$ at early times when the Lo domains are small compared to the actin mesh size

(≈1 μm), while at later times, larger domains are driven to grow more rapidly (Fig. S3 [9]).

We compare these active data to control experiments in which lipid bilayers without actin are heated above the miscibility temperature and then allowed to cool so that the domains can reform and coarsen (Supplemental Material [9], Video S1). Figure 2 (black closed symbols) shows that passive membranes recover the scaling of $\alpha = 1/3$, which applies to both coalescence and evaporation-condensation mechanisms of coarsening and has been well established for membrane domains in both experimental and theoretical work [4,5,7,10] (see Supplemental Material for derivation). We perform these passive experiments with five different lipid compositions, including critical mixtures, obtaining scaling results consistent with those of Stanich *et al.* on GUVs (Supplemental Material [9], Figs. S1 and S4) [7]. We hypothesize that actin contraction generates in-plane forces in the membrane, which drive the lipid domains to grow at an accelerated rate.

Theory.—To evaluate our hypothesis that active convection can accelerate domain coarsening, we use a Cahn-Hilliard model to evolve a phase-separating 2D system under surface flows. We evolve a concentration order parameter $\phi(\mathbf{x}, t)$ using the Cahn-Hilliard equation [23], which is commonly used to study coarsening in binary mixtures [24–27]. The Cahn-Hilliard model predicts the passive growth exponent $\alpha = 1/3$ (Fig. 2, green closed circles and Supplemental Material [9], Video S3), which is consistent with prior work on Ostwald ripening in the absence of flow [4,28] (see Supplemental Material).

To analyze the effect of 2D active flows on domain coarsening, we present the following nondimensional Cahn-Hilliard equation in Fourier space:

$$\frac{d\phi_k}{dt} + \mathrm{Pe}\mathcal{F}\{\mathbf{v}\cdot\nabla\phi\} = -k^2\mathcal{F}\left\{\frac{\delta f}{\delta\phi}\right\} - k^4\phi_k, \qquad (1)$$

where ϕ_k is the Fourier transform of $\phi(\mathbf{x}, t)$, k is the wave vector, $\mathbf{v}$ is the nondimensional convective surface velocity generated by the actin filaments, the Péclet number $\mathrm{Pe} \equiv \dot{\gamma}\kappa/M$, $\dot{\gamma}$ is the rate of strain, M is lipid mobility, and κ is a surface tension parameter. We model the bulk free energy, $f[\phi(\mathbf{x}, t)] = \phi^4/4 - \phi^2/2$, a double-well potential where the concentration of pure phases is $\phi = \pm 1$. We add a convective term $\mathbf{v}\cdot\nabla\phi$ to impose surface flows on the phase-separating system, testing the effect of our hypothesized actin-induced surface convection on domain coarsening. We use this model to obtain a mechanistic understanding of how active convection impacts the kinetics of domain growth. Hydrodynamic effects of the fluid and the bulk Ld phase may also be included, but we omit them here because surface tension (or line tension) driven flows that cause accelerated coarsening mechanisms are only significant for near-critical point quenches where the minority phase is elongated and/or interconnected [11,29].

We numerically solve the Cahn-Hilliard model using pseudospectral methods with periodic boundary conditions, starting from an initial state ϕ_0 with uniform noise. To avoid any boundary artifacts, we restricted our analysis to the interior of the simulation box (see Supplemental Material [9], Fig. S6). To corroborate our experimental results, we impose the surface flow field obtained by PIV analysis of actin [Fig. 1(d), white arrows]. We fix Cahn-Hilliard parameters M and κ based on the pixel resolution of the camera, while varying Pe to evaluate the effect of active flows on growth rate (Supplemental Material [9], Video S4). Figure 2 (green symbols) shows that domains coarsen rapidly for the strongest flows ($\alpha = 0.93$ for $\mathrm{Pe} = 10^{-2}$), while weaker flows effectively act as noise and recover passive scaling ($\alpha = 0.34$ for $\mathrm{Pe} = 10^{-4}$). The experimentally derived scaling exponents of $\alpha = 0.59$–0.74 lie between those for $\mathrm{Pe} = 10^{-4}$ and $\mathrm{Pe} = 5 \times 10^{-3}$ in the numerical solutions. These results are consistent with an estimate of the molecular Péclet number based on literature values, $\approx 10^{-4}$–10^{-3}, using ≈1 nm lipids with diffusivity 1–10 $\mu\mathrm{m}^2/\mathrm{s}$ under surface flows with velocity ≈1 μm/s [30,31].

In addition to the Ostwald ripening mechanism in the Cahn-Hilliard model, we note that a different model of phase coarsening based on the Smoluchowski coagulation model predicts a $\alpha = 2/3$ growth for domains subjected to weak shear flows. The Smoluchowski coagulation model is commonly used to predict Brownian flocculation of colloids [32] and diffusion-reaction dynamics of macromolecules [33] and is conceptually distinct from the molecular mechanisms driving coarsening in the Cahn-Hilliard equation. In the Smoluchowski perspective, the lipid domains are modeled as macroscopic colloids of fixed size that merge upon contact (i.e., dimerize via an infinitely fast chemical reaction upon contact) [11]. Thus, although they both predict $\alpha = 1/3$ passive scaling, the Smoluchowski model assumes domain growth via coalescence as opposed to Ostwald ripening [8,34].

To obtain the enhanced scaling in shear flow under the Smoluchowski perspective, we consider the conservation of the number density n of singlet domains,

$$\frac{dn}{dt} + J = 0, \qquad (2)$$

where J is a sink that captures the merging of singlet domains to dimerized domains,

$$J = -\frac{D_c}{a} n^2 \oint_{r=2a} \mathbf{n}\cdot(\mathrm{Pe}_c\mathbf{v} - \nabla_r \ln g + \nabla_r V) g \, d\ell. \qquad (3)$$

The sink depends on the contact integral over the arc length $d\ell$ of the normalized pair distribution of domains $g(\mathbf{r}; \mathrm{Pe}_c)$,

nondimensional velocity field $\mathbf{v}$, unit normal to the domain surface $\mathbf{n}$, nondimensional pair potential V, gradient operator relative to the center of a domain ∇_r, and Péclet number based upon treating the domains as colloids $\mathrm{Pe_c} \equiv \dot{\gamma} a^2 / D_c$ (with domain diffusivity D_c). Assuming that the pair distribution quickly reaches a steady state at all times compared to the decay of the singlet density (quasistatic approximation), we solve for $g(\mathbf{r}; \mathrm{Pe_c})$ with boundary conditions $g = 0$ at contact and $g = 1$ far away. The $g = 0$ condition at contact assumes an instantaneously fast merging of two singlet domains, although a finite reaction time is also straightforward to implement. Hydrodynamic interactions between the domains may also be included in the pair distribution problem, but we omit them here because lubrication flows can generally only slow down the collision rates between membrane domains [11,35].

Equations (2) and (3) show that the singlet density decreases by a second-order reaction, $J = k^{\mathrm{eff}} n^2$, where k^{eff} is interpreted as the transport-limited effective reaction rate constant. Assuming the domains are circular with no bulk interaction ($V = 0$), subjected to a simple shear flow, a perturbation analysis at small $\mathrm{Pe_c}$ gives

$$k^{\mathrm{eff}} = \frac{\pi k_B T}{8 \eta a \ln\left(\frac{L}{2a}\right)} \left(1 + C \mathrm{Pe_c}^{1/2}\right), \tag{4}$$

with bulk solvent viscosity η, system size L, and a numerical prefactor C (see Supplemental Material [9]) [32,36,37]. We have used the Saffman-Delbrück diffusivity for large domains compared to the Saffman-Delbrück length [38]; the membrane is embedded within a bulk 3D fluid, and the quasi-2D geometry is critical for obtaining the correct scaling [7,8,39]. For a constant domain area fraction $\phi_A = n\pi a^2$, Eqs. (2)–(4) yield a domain growth scaling of $a(t) \sim t^{1/3}$ in the absence of flow ($\mathrm{Pe_c} = 0$) and an enhancement in the presence of weak shear flows $a(t) \sim t^{2/3}$. Therefore, both the coalescence-based Smoluchowski model and the ripening-based Cahn-Hilliard model predict a similar enhancement to the growth of domains with active convection; both mechanisms are present in the experiments.

Returning to the Cahn-Hilliard model [Eq. (1)], we also considered simple toy models of the surface velocity to gain a more mechanistic understanding of the effect of flows on domain growth. We consider a general 2D linear flow $\mathbf{v}(\mathbf{x}) = \mathbf{G} \cdot \mathbf{x}$, where $\mathbf{G}$ is a gradient tensor. We compute Eq. (1) for shear and rotational flow fields and measure the domain size and structure as a function of time. In shear flow, we observed frequent domain merging and elongation along the extensional axis of shear [Fig. 3(a), Supplemental Material [9], Video S5]. Figure 3(c) shows that, as the static structure factor evolves in time, the magnitudes of the peaks grow as the peaks shift toward lower wave vectors.

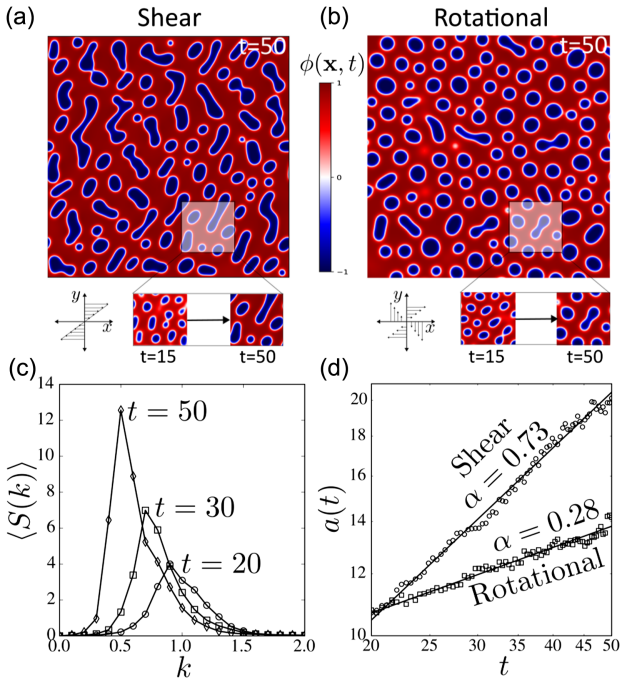

FIG. 3. General linear flows modulate the growth and morphology of phase-separating domains. Numerical solution snapshots of phase separation for Eq. (1) in (a) shear flow and (b) rotational flow. Insets: evolution of the domains. (c) Static structure factor for domains under shear flow. (d) Shear flow increases the domain growth rate, whereas rotational flow maintains the same scaling as passive Ostwald ripening, $\approx t^{1/3}$. The parameters shown here correspond to $(M, \kappa, \dot{\gamma}) = (1, 0.25, 0.04)$, or $\mathrm{Pe} = 10^{-2}$.

Previous work shows that mechanical shear enhances droplet coarsening at low Péclet numbers in both 2D and 3D systems, particularly along the extensional axis of shear [12,14,40], which we also observe at long times (Supplemental Material [9], Video S6). We hypothesize that, with one fewer spatial degree of freedom than 3D systems, our quasi-2D geometry enhances the effect of flow-accelerated coarsening, as there is one fewer unsheared mode of relaxation available to the domains.

Conversely, in rotational flow, the domains remain approximately circular, similar to the passive case [Fig. 3(b), Supplemental Material [9], Video S5]. In Fig. 3(d), we compare the rate of domain growth for the two linear flows, finding that at high $\mathrm{Pe} = 10^{-2}$, shear flow accelerates domain growth ($\alpha = 0.73$), while rotational flow essentially recovers passive scaling ($\alpha = 0.28$). This result is consistent with the physical intuition that rigid body rotation about the center of the system should not alter the frequency of collisions between domains. Our analysis provides further physical insight into our experiments, as any arbitrary linear flow may be constructed from linear combinations of shear and rotational flow. For example, extensional flow is a sum of shear flow and rotational flow,

has features that are similar to the flows observed in our experiments, and also yields $\alpha \approx 0.73$ scaling.

Both the Smoluchowski and Cahn-Hilliard models predict a $\alpha \approx 2/3$ enhancement in simple shear flow, but no enhancement in rotational flow. We note that coalescence is an important mechanism of growth in the experiments due to the large colloidal Péclet number $\mathrm{Pe}_c \equiv \dot{\gamma} a^2/D_c \approx 10$, compared to the molecular Péclet considered in the Cahn-Hilliard model, $\mathrm{Pe} \equiv \dot{\gamma}\kappa/M \approx 10^{-4}$–$10^{-2}$.

While numerical solutions validate that 2D flows accelerate domain growth, we can obtain further mechanistic insight by linearizing the Cahn-Hilliard equation and obtaining an analytical approximation of α at early times. Under simple shear flow, perturbation analysis at small Pe yields $a(t) \sim t^{1/4} + \mathrm{Pe} t^{5/4} + \mathcal{O}(\mathrm{Pe}^2)$ (see Supplemental Material [9]). Note that the passive scaling obtained from the linearized equation is $t^{1/4}$, which is different from the $t^{1/3}$ scaling obtained from the numerical solution to the fully nonlinear equation (1). This is consistent with prior studies of the Cahn-Hilliard equation in the context of the kinetics of Ostwald ripening [27]. The linearized form captures domain growth at very early times, and nonlinear terms are required to observe $t^{1/3}$ passive scaling. Nonetheless, even in the linearized form, this calculation demonstrates that the leading-order effect of flows appears at $\mathcal{O}(t^{5/4})$, and any surface flows will accelerate the growth scaling beyond the passive exponent. While not exact solutions, these trends are consistent with our experimental observations that surface flows can significantly accelerate the kinetics of coarsening.

This material is based upon work supported by the National Science Foundation under Grant No. 2150686. D. P. A. is supported by the National Science Foundation Graduate Research Fellowship under Grant No. 2139319. S. C. T. is supported by the Packard Fellowship in Science and Engineering by The David and Lucile Packard Foundation.

*D. P. A. and A. G. contributed equally to this work.
†stakatori@ucsb.edu

[1] B. Alberts, A. Johnson, J. Lewis, M. Raff, K. Roberts, and P. Walter, *Molecular Biology of the Cell*, 3rd ed. (Taylor & Francis Group, London, 2007).
[2] R. Phillips, J. Kondev, J. Thierot, and H. Garcia, *Physical Biology of the Cell*, 2nd ed. (Garland Science, Taylor & Francis Group, London, 2012).
[3] S. L. Veatch and S. L. Keller, Biophys. J. **85**, 3074 (2003).
[4] I. Lifshitz and V. Slyozov, J. Phys. Chem. Solids **19**, 35 (1961).
[5] B. A. Camley and F. L. H. Brown, J. Chem. Phys. **135**, 225106 (2011).
[6] B. A. Camley and F. L. H. Brown, Phys. Rev. Lett. **105**, 148102 (2010).
[7] C. A. Stanich, A. R. Honerkamp-Smith, G. G. Putzel, C. S. Warth, A. K. Lamprecht, P. Mandal, E. Mann, T. A. D. Hua, and S. L. Keller, Biophys. J. **105**, 444 (2013).
[8] V. Frolov, Y. Chizmadzhev, F. Cohen, and J. Zimmerberg, Biophys. J. **91**, 189 (2006).
[9] See Supplemental Material at http://link.aps.org/supplemental/10.1103/PhysRevLett.131.128402 for experimental and simulation videos, detailed experimental and simulation protocols, domain growth scaling derivations, and supplemental figures.
[10] C. Wagner, Z. Elektrochem. Ber. Bunsenges. Phys. Chem. **65**, 581 (1961).
[11] E. D. Siggia, Phys. Rev. A **20**, 595 (1979).
[12] T. Ohta, H. Nozaki, and M. Doi, J. Chem. Phys. **93**, 2664 (1990).
[13] Z. Shou and A. Chakrabarti, Phys. Rev. E **61**, R2200 (2000).
[14] A. J. Bray, Phil. Trans. R. Soc. A **361**, 781 (2003).
[15] M. I. Angelova and D. S. Dimitrov, Faraday Discuss. Chem. Soc. **81**, 303 (1986).
[16] A. D. Edelstein, M. A. Tsuchida, N. Amodaj, H. Pinkard, R. D. Vale, and N. Stuurman, J. Biol. Methods **1**, e10 (2014), https://pubmed.ncbi.nlm.nih.gov/25606571.
[17] J. A. Spudich and S. Watt, J. Biol. Chem. **246**, 4866 (1971).
[18] C. F. E. Schroer, L. Baldauf, L. van Buren, T. A. Wassenaar, M. N. Melo, G. H. Koenderink, and S. J. Marrink, Proc. Natl. Acad. Sci. U.S.A. **117**, 5861 (2020).
[19] S. MacLean-Fletcher and T. D. Pollard, Biochem. Biophys. Res. Commun. **96**, 18 (1980).
[20] S. S. Margossian and S. Lowey, in *Methods in Enzymology* (Elsevier, New York, 1982), Vol. 85, pp. 55–71.
[21] A. Tian, C. Johnson, W. Wang, and T. Baumgart, Phys. Rev. Lett. **98**, 208102 (2007).
[22] T. Baumgart, S. T. Hess, and W. W. Webb, Nature (London) **425**, 821 (2003).
[23] J. W. Cahn, J. Chem. Phys. **42**, 93 (1965).
[24] P. K. Inguva, P. J. Walker, H. W. Yew, K. Zhu, A. J. Haslam, and O. K. Matar, Soft Matter **17**, 5645 (2021).
[25] S. J. Watson, F. Otto, B. Y. Rubinstein, and S. H. Davis, Physica (Amsterdam) **178D**, 127 (2003).
[26] L. Ó Náraigh and J.-L. Thiffeault, Phys. Rev. E **75**, 016216 (2007).
[27] B. König, O. J. J. Ronsin, and J. Harting, Phys. Chem. Chem. Phys. **23**, 24823 (2021).
[28] A. J. Bray and C. L. Emmott, Phys. Rev. B **52**, R685 (1995).
[29] D. R. Tree, K. T. Delaney, H. D. Ceniceros, T. Iwama, and G. H. Fredrickson, Soft Matter **13**, 3013 (2017).
[30] K. J. Seu, A. P. Pandey, F. Haque, E. A. Proctor, A. E. Ribbe, and J. S. Hovis, Biophys. J. **92**, 2445 (2007).
[31] R. Macháň and M. Hof, Biochim. Biophys. Acta **1798**, 1377 (2010).
[32] W. B. Russel, D. A. Saville, and W. R. Schowalter, *Colloidal Dispersions* (Cambridge University Press, Cambridge, England, 1989).
[33] G. H. Fredrickson and L. Leibler, Macromolecules **29**, 2674 (1996).
[34] B. A. Camley and F. L. H. Brown, J. Chem. Phys. **135**, 225106 (2011).

[35] N. Oppenheimer and H. A. Stone, Biophys. J. **113**, 440 (2017).
[36] L. G. Leal, *Advanced Transport Phenomena* (Cambridge University Press, Cambridge, England, 2007).
[37] W. M. Deen, *Introduction to Chemical Engineering Fluid Mechanics*, Cambridge Series in Chemical Engineering (Cambridge University Press, Cambridge, England, 2016).
[38] P. G. Saffman and M. Delbrück, Proc. Natl. Acad. Sci. U.S.A. **72**, 3111 (1975).
[39] S. Ramachandran, S. Komura, and G. Gompper, Europhys. Lett. **89**, 56001 (2010).
[40] F. Corberi, G. Gonnella, and A. Lamura, Phys. Rev. E **62**, 8064 (2000).

SUPPLEMENTAL MATERIAL:
Active surface flows accelerate the coarsening of lipid membrane domains

Daniel P. Arnold,* Aakanksha Gubbala,* and Sho C. Takatori†
Department of Chemical Engineering, University of California, Santa Barbara, Santa Barbara, CA

I. MOVIE DESCRIPTION

Movie S1: Passive domain coarsening is observed experimentally on a phase-separated lipid bilayer. A single-phase planar lipid membrane was previously heated to $\approx 37°$C, and is shown here as it cools to room temperature. Liquid-ordered domains (green) nucleate and coarsen as the membrane cools in the absence of flow.

Movie S2: Actomyosin-driven flows accelerate lipid domain coarsening on an experimental planar bilayer. (*Upper left*) Liquid-ordered domains (green) are initially arrested by actin, but rapidly change morphology and grow when activity is triggered at $t = 0$. (*Upper right*) An actomyosin cortex adsorbed to the lipid membrane via electrostatic attractions begins to contract when adenosine triphosphate (ATP) is introduced at $t = 0$. Actin is pulled inward toward a central cluster as it contracts. This actin cluster appears to delaminate from the surface allowing domains to coalesce in its wake. (*Lower*) Actin (magenta) and lipid domain (green) images are superimposed upon one another.

Movie S3: Numerical simulation of Cahn-Hilliard model for passive coarsening. The model parameters are (M, κ)=(1, 0.25).

Movie S4: Numerical simulations of Cahn-Hilliard model with experimentally obtained actin flow fields at Pe $= 10^{-2}$ (*left*), Pe $= 5 \times 10^{-3}$ (*center*), and Pe $= 10^{-4}$ (*right*). The model parameters are (M, κ)=(300, 16).

Movie S5: Numerical simulations of Cahn-Hilliard model with shear flow (*left*), and rotational flow (*right*). The model parameters are (M, κ, $\dot{\gamma}$)=(1, 0.25, 0.04), which correspond to Pe $= 10^{-2}$.

Movie S6: Numerical simulations of Cahn-Hilliard model with shear flow, run for longer time than Movie S5 (*left*). At long times, domains clearly begin to elongate along the extensional axis of the shear flow. The model parameters are (M, κ, $\dot{\gamma}$)=(1, 0.25, 0.04), which correspond to Pe $= 10^{-2}$.

In movies S3-6, the simulation timescale is non-dimensionalized by the characteristic time scale of the Cahn-Hilliard model, $t_c = \kappa/M$. The timestamps in movies S3 and S4 are scaled by 10 to match with the timescale of the experiments.

II. DETAILED EXPERIMENTAL METHODS

A. Buffers

Filamentous actin buffer (F-buffer) consists of 50 mM Tris (pH 7.5), 2 mM magnesium chloride, 0.5 mM adenosine triphosphate (ATP), 0.2 mM calcium chloride, 25 mM potassium chloride, and 1 mM dithiothreitol (DTT). DTT was added to all buffers immediately before use to preserve its reactivity.

Assay buffer (A-buffer) consists of 25 mM imidazole (pH 7.4), 4 mM magnesium chloride, 1 mM (ethylene glycol-bis(β-aminoethyl ether)-N,N,N',N'-tetraacetic acid) (EGTA), 25 mM potassium chloride, and 1 mM DTT.

Globular actin buffer (G-buffer) consists of 2 mM Tris (pH 8.0), 0.2 mM calcium chloride, 0.5 mM DTT, 1 mM sodium azide, and 0.2 mM ATP.

B. Actin and myosin preparation

Rabbit skeletal muscle actin was purified from muscle acetone powder (Pel-Freez, catalog no: 41995-2, Lot 16743) using standard methods [1, 2]. No rabbits or other animals were directly involved in this study. Actin was stored as

* These authors contributed equally to this work

† stakatori@ucsb.edu

depolymerized globular actin (G-actin) at -80°C in G-buffer with 6% sucrose until use.

Actin was labeled with fluorescent Alexa Fluor 555 NHS Ester (Succinimidyl Ester) (Invitrogen catalog no: A20009) for microscopic visualization. G-actin was reacted with NHS-Alexa Fluor 555 in HEPES buffer at room temperature for 30 minutes. 2x-concentrated F-buffer was then added to the G-actin, quenching the NHS reaction and causing G-actin to polymerize to F-actin. F-actin polymerization proceeded for 30 minutes at room temperature, and then overnight at 4°C. Labeled F-actin was centrifuged at 142,000 × g for 30 minutes, and the pellet collected. Unreacted dye and defective G-actin monomers and oligomers that were unable to polymerize were discarded in the supernatant. Labeled F-actin was dissolved in G-buffer, and allowed to de-polymerize for three days at 4°C before freezing and storing in 6% sucrose at -80°C.

Rabbit skeletal muscle myosin II and heavy meromyosin (HMM) were purified from rabbit skeletal muscle (Pel-Freez Biologicals, Rogers, Arkansas) using standard methods [3]. Myosin II was frozen in 150 mM potassium phosphate buffer (pH 7.5) with 6% sucrose and 10 mM EDTA at -80°C until use. HMM was frozen in 10 mM potassium phosphate buffer (pH 7.0), 100 mM potassium chloride, 0.3 mM EGTA, 1 mM DTT, and 6% sucrose at -80°C until use.

C. Giant unilamellar vesicle (GUV) preparation

Giant unilamellar vesicles (GUVs) were prepared using the established method electroformation [4]. Briefly, lipids were mixed with the following composition: 44.7% 1,2-dioleoyl-sn-glycero-3-phosphocholine (DOPC, Avanti catalog no: 850375P), 34.7% 1,2-dipalmitoyl-sn-glycero-3-phosphocholine (DPPC, Avanti catalog no: 850355C), 15% cholesterol (TCI Chemical, catalog no: C3624), 5% 1,2-dioleoyl-3-trimethylammonium-propane (DOTAP, Avanti catalog no: 890890P), 0.3% 1,2-distearoyl-sn-glycero-3-phosphoethanolamine-N-[poly(ethylene glycol)2000-N'-carboxyfluorescein] (DSPE-PEG2k-FITC, Avanti catalog no: 810120C), and 0.3% ATTO 647-labeled 1,2-dioleoyl-sn-glycero-3-phosphoethanolamine (ATTO 647-DOPE, ATTO-TEC catalog no: AD 647-161). Compositional variations were achieved by sampling different vesicles within the diverse population that formed under these conditions. An additional set of vesicles was formed using 52.7% DOPC, 24.7% DPPC, 8% DOTAP, 0.3% DSPE-PEG2k-FITC, and 0.3% ATTO 647-DOPE, to achieve the lowest area fraction sampled amongst the active samples. Lipids were spread on an indium tin oxide (ITO)-coated microscope slide (Diamond Coatings, 8-12 Ohm slide) and dried under vacuum for 30 minutes.

A 2 mm rubber gasket was sandwiched between the ITO-coated slide containing lipids and a clean ITO-coated slide, and the interstitial space filled with 75 mM sucrose solution. A sinusoidal electric potential of amplitude 3V (peak-to-peak) and frequency 10 Hz was applied to the chamber for two hours at 50 °C. After two hours, the frequency was changed to 2 Hz for 30 minutes. The resulting GUVs were collected, stored at room temperature and used within one day.

D. Surface preparation

Glass cover slips No. 1.5 (Fisher) were cleaned with piranha solution (3:1 sulfuric acid:hydrogen peroxide) for five minutes and then washed with deionized water. The cover slips were then made hydrophobic via reaction with trimethylchlorosilane (Sigma) vapors in a vacuum chamber, under house vacuum for ten minutes. A 6 mm cylindrical polydimethylsiloxane (PDMS) chamber was attached to the cover slip surface to hold liquids. Cover slips were incubated with 200 nM heavy meromyosin (HMM) for five minutes. After five minutes, 0.1 mg/mL polylysine-grafted-PEG (PLL-g-PEG) was added and the HMM/PLL-g-PEG solution incubated for another five minutes. The coverslip was then washed, first with A-buffer, and then with MilliQ water.

E. Assembling actomyosin cortex on a lipid bilayer

GUVs in MilliQ water were added to the cover slip chamber. The cover slip was heated to 37°C for at least 20 minutes, during which time GUVs ruptured on the treated surface. Unbound GUVs were then washed from the cover slip with A-buffer. For experiments with activity, the cover slip was then incubated in 1 µM F-actin for 10 minutes at 37 °C. F-actin spontaneously adsorbed to the liquid-ordered phase of lipid bilayer via electrostatic attraction to DOTAP [5]. Unbound actin was washed from the cover slip with A-buffer. The cover slip with lipids and actin was incubated in 500 nM Myosin II for ten minutes at 37°C before the unbound myosin II washed away with A-buffer.

F. Microscope for all imaging experiments

All imaging was carried out on an inverted Nikon Ti2-Eclipse microscope (Nikon Instruments) using an oil-immersion objective (Apo 100x, NA 1.45, oil). Lumencor SpectraX Multi-Line LED Light Source was used for excitation (Lumencor, Inc). Fluorescent light was spectrally filtered with emission filters (432/36, 515/30, 595/31, and 680/42; Semrock, IDEX Health and Science) and imaged on a Photometrics Prime 95 CMOS Camera (Teledyne Photometrics). Microscope images were collected using MicroManager 1.4 software [6].

G. Imaging passive domain growth

Planar lipid membranes without actin were gently heated with a hair dryer until the domains melted, as confirmed by fluorescence microscopy. The hair dryer was then withdrawn, and the bilayer imaged over time as it cooled and the domains re-formed and grew.

H. Imaging active domain growth

Due to the temperature-sensitivity of the actin-membrane interactions, actomyosin cortex, and DMNPE-caged ATP, active domain growth was tracked at room temperature. Thus, domains were tracked as they grew from a small initial size, fixed by the actin network, to a larger size under the influence of actomyosin activity.

Photosensitive caged ATP (1µM DMNPE-caged ATP, Invitrogen catalog no: A1049) was added to planar lipid membranes with actin and myosin before imaging. The sample was irradiated with a brief (<1 s) pulse of 404 nm light, converting the caged ATP to usable ATP. Domains and actin were then imaged over time, as the actomyosin contracted, and the domain size and morphology evolved.

I. Image analysis

Microscope images of lipid domains were thresholded in ImageJ and the area and perimeter of the resulting black and white images calculated using MATLAB (MathWorks). Characteristic domain size a was taken to be the ratio of area/perimeter. Domain size versus time was fitted to an equation of the form:

$$a = (At + B)^{\alpha} \tag{1}$$

where the prefactor A is related to solvent viscosity, substrate friction, and domain area fraction; B is related to the initial size at $t = 0$, $a_0 = B^{\alpha}$; and α is the growth rate exponent. For plots of domain size versus time in Fig. 2 of the main text, time is shifted for each experimental realization, so that $t = 0$ corresponds to the point at which $a = 0$. Thus, $t_{\text{plot}} = t + \frac{B}{A}$ where $t = 0$ is the time at which imaging begins, and $t_{\text{plot}} = 0$ is the time at which domains begin to form.

III. THEORY OF DOMAIN GROWTH

In this section we discuss multiple theoretical approaches to predict the growth rate of lipid domains. We first derive the domain growth rate via a Cahn-Hilliard field-based approach in which we describe the evolution of an order parameter ϕ, as described by Lifshitz and Slyozov [7, 8]. This approach assumes that domains grow solely via molecular transport, i.e. an evaporation/condensation of Ostwald ripening mechanism.

We then derive the rate of domain growth via a Smoluchowski agent-based approach, in which we treat the domains as individual particles [9]. By treating particle coalescence as a severely transport-limited two-species reaction, we show that domains grow at the same rate via coalescence, as they do via evaporation/condensation. Finally, by applying a simple shear flow to this Smoluchowski-based description, we demonstrate that 2D flows can increase the rate of domain coarsening.

A. Lifshitz-Slyozov Scaling

Consider a domain of radius a and concentration, $\phi = +1$, surrounded by bulk concentration phase, $\phi = -1$. The interface has line tension σ. In the bulk phase, there is a fluctuation $\varepsilon(r)$ because the concentration is not uniformly

$\phi = -1$ near $r = a$. Assume $\phi(r) = -1 + \varepsilon(r)$, $\varepsilon \ll 1$, and the gradients of order parameter in the bulk phase is negligible. The Cahn-Hilliard model now becomes $\partial_t \varepsilon = 2\nabla^2 \varepsilon + \mathcal{O}(\varepsilon^2)$. Assuming that the fluctuations quickly reach a steady state at all times compared to the growth of domains (quasi-static approximation), we get

$$\nabla^2 \varepsilon = 0 \ . \tag{2}$$

The solution to Eq. 2 is given by

$$\varepsilon(r) = C_1 \ln(r) + C_2 \tag{3}$$

where C_1 and C_2 are integration constants. We use the boundary conditions $\varepsilon(r = a) = \sigma/(2a)$ and $\varepsilon(r = L) = 0$ (where L is the box length) to solve for C_1 and C_2 in Eq. 3 to obtain.

$$\varepsilon(r) = \frac{\sigma}{2a} \frac{\ln(r/L)}{\ln(a/L)} \ . \tag{4}$$

The droplet radius grows according to $\mathrm{d}a/\mathrm{d}t$. Performing a flux balance at the interface gives

$$j = -2\nabla \varepsilon|_{r=a} = \Delta\phi \frac{\mathrm{d}a}{\mathrm{d}t} \tag{5}$$

where j is the surface flux and $\Delta\phi = 2$ is the difference in order parameter across the interface. Thus,

$$\frac{\mathrm{d}a}{\mathrm{d}t} = -\frac{\sigma}{2a^2 \ln(a/L)} \ . \tag{6}$$

Solving this first order differential equation yields

$$\frac{a^3}{9}\left[1 + 3\ln\left(\frac{L}{a}\right)\right] = \frac{\sigma}{2} t + C \tag{7}$$

where C is an integration constant. In the late stages of coarsening, this constant is small compared to the first term on the right-hand side. Further, as $t \to \infty$, $a \to L$. In this limit, we can write $L/a = 1 + \epsilon$, where $\epsilon \ll 1$. Eq. 7 becomes

$$\frac{a^3}{9}\left[1 + 3\ln(1 + \epsilon)\right] = \frac{\sigma}{2} t \ . \tag{8}$$

The series expansion of the log term on the left-hand side is

$$\ln(1 + \epsilon) = \epsilon + \mathcal{O}(\epsilon^2) \ . \tag{9}$$

By substituting Eq. 9 in Eq. 8, we get

$$\frac{a^3}{9}(1 + 3\epsilon) = \frac{\sigma}{2} t \ . \tag{10}$$

The leading order solution is

$$a^3 = \frac{9}{2}\sigma t \ . \tag{11}$$

Thus, the domains grow as $a(t) \sim t^{1/3}$ in 2D for Ostwald ripening.

B. Smoluchowski Coalescence

Domain growth via coalescence can be described following Siggia [10] and the Smoluchowski coagulation model, which is used to model the flocculation of colloids of a fixed size. Here we first adapt the Smoluchowski description of colloid flocculation to calculate the growth rate of singlet domains in the absence of flow (passive). This approach has been previously applied to lipid domain growth by Frolov et al. [11], and treats domains as particles of uniform size, which merge infinitely quickly and irreversibly upon contact. We then apply a simple shear flow to the 2D system and find the dependence of the domain growth rate on the colloidal Péclet number $\mathrm{Pe_c}$, as described by Russel, Saville, and Schowalter [9] for 3D colloidal aggregation.

1. Passive domain growth in the absence of flow

To model the growth of 2D passive domains in the absence of flow, we consider two identical circular particles (particles 1 and 2) of size a and colloidal scale diffusivity D_c. These particles represent singlet lipid domains. This pair of particles has the pair distribution function $g(\mathbf{r}, t)$, which evolves according to the Smoluchowski equation (given here in dimensional form):

$$\frac{\partial g}{\partial t} + \nabla_x \cdot \mathbf{j}_1 + \nabla_r \cdot (\mathbf{j}_1 - \mathbf{j}_2) = 0 \tag{12}$$

where $\mathbf{j}_i$ denotes the flux of species i, ∇_x is the gradient operator relative to the origin, and ∇_r is the gradient operator relative to the center of particle 1. Assuming spherical particles and spatial invariance, Eq. 12 becomes

$$\frac{\partial g}{\partial t} + \nabla_r \cdot \mathbf{j}_\mathrm{rel} = 0 \tag{13}$$

where $\mathbf{j}_\mathrm{rel} = \mathbf{j}_1 - \mathbf{j}_2$. We define $\mathbf{j}_\mathrm{rel}$ as

$$\mathbf{j}_\mathrm{rel} = \mathbf{U}g - D_\mathrm{c}\left(\nabla_r g + g\frac{\nabla_r V}{k_\mathrm{B}T}\right) \tag{14}$$

where $\mathbf{U}$ is bulk fluid velocity and V is the inter-particle potential. In the absence of flow, $\mathbf{U} = \mathbf{0}$ and

$$\mathbf{j}_\mathrm{rel} = -D_\mathrm{c}\left(\nabla_r g + g\frac{\nabla_r V}{k_\mathrm{B}T}\right) \tag{15}$$

for all $r \geq 2a$. Hydrodynamic interactions between the domains may also be included in the pair distribution problem, but we omit them here because lubrication flows can generally only slow down the collision rates between membrane domains [10, 12].

Integrating Eq. 13 over all space gives

$$\frac{\partial n}{\partial t} + \int \nabla_r \cdot \mathbf{j}_\mathrm{rel}\ \mathrm{d}\mathbf{r} = 0 \tag{16}$$

where n is the number density of singlet domains, defined as $n(t) = \int g(\mathbf{r}, t)\ \mathrm{d}\mathbf{r}$. Applying the divergence theorem converts the integral over all space in Eq. 16 into a line integral over the perimeter of domain 1:

$$\int \nabla_r \cdot \mathbf{j}_\mathrm{rel}\ \mathrm{d}\mathbf{r} = \oint_{r=2a} \mathbf{n} \cdot \mathbf{j}_\mathrm{rel}\ \mathrm{d}\ell \tag{17}$$

where $\mathbf{n}$ is the normal vector and $\mathrm{d}\ell$ is an integral over the perimeter at domain contact. Assuming a steady state flux of domains at the surface of species 1 makes Eq. 17 equal to a constant

$$J = \oint_{r=2a} \mathbf{n} \cdot \mathbf{j}_\mathrm{rel}\ \mathrm{d}\ell. \tag{18}$$

Thus the number density of domains evolves in time according to

$$\frac{\partial n}{\partial t} = -J\ . \tag{19}$$

To find $g(r)$ and thus ultimately solve for J, we solve Eq. 13, which reduces to

$$\frac{\mathrm{d}}{\mathrm{d}r}\left[r\left(\frac{\mathrm{d}g}{\mathrm{d}r} + g\frac{\mathrm{d}\left(V/k_\mathrm{B}T\right)}{\mathrm{d}r}\right)\right] = 0 \tag{20}$$

for a radially symmetric system at steady state, with a flux defined by Eq. 15. Applying the boundary conditions $g(r = 2a) = 0$ and $g(r = L) = n^2$ for a large, but finite system size L gives the solution

$$g(r) = \frac{n^2 e^{-V/k_\mathrm{B}T}\int_{2a}^{r} \frac{e^{V/k_\mathrm{B}T}}{r}\mathrm{d}r}{\int_{2a}^{L} \frac{e^{V/k_\mathrm{B}T}}{r}\mathrm{d}r}. \tag{21}$$

Treating the domains as hard circles such that $V(r \geq 2a) = 0$ gives

$$g(r \geq 2a) = \frac{\ln\left(\frac{r}{2a}\right)}{\ln\left(\frac{L}{2a}\right)} n^2. \tag{22}$$

Plugging Eq. 22, evaluated at the colloid surface $r = 2a$, into Eq. 15, and then substituting into Eq. 18, gives

$$J = 4\pi a D_{\mathrm{c}} \left.\frac{\mathrm{d}g}{\mathrm{d}r}\right|_{r=2a} = \frac{2\pi D_{\mathrm{c}} n^2}{\ln\left(\frac{L}{2a}\right)}. \tag{23}$$

Substituting Eq. 23 into Eq. 19 and applying the diffusivity $D_{\mathrm{c}} = \frac{k_{\mathrm{B}}T}{16\eta a}$ for 2D domains much larger than the Saffman-Delbrück limit, $a \gg L_{\mathrm{SD}}$ [13], gives

$$\frac{\mathrm{d}n}{\mathrm{d}t} = -\frac{\pi k_{\mathrm{B}} T}{8\eta a \ln\left(\frac{L}{2a}\right)} n^2 \tag{24}$$

where and η is the 3D solvent viscosity.

Assuming a constant area fraction of domains, $\phi_{\mathrm{A}} = \pi a^2 n$, we rewrite Eq. 24 to describe the evolution of domain size a:

$$\frac{\mathrm{d}a}{\mathrm{d}t} = \frac{k_{\mathrm{B}} T \phi_{\mathrm{A}}}{16\eta a^2 \ln\left(\frac{L}{2a}\right)}. \tag{25}$$

For lipid domains of initial size a_0 at $t = 0$, the solution to Eq. 24 is

$$\frac{1}{9}a^3\left[3\ln\left(\frac{L}{2a}\right)+1\right] - \frac{1}{9}a_0^3\left[3\ln\left(\frac{L}{2a_0}\right)+1\right] = \frac{k_{\mathrm{B}}T\phi_{\mathrm{A}}}{16\eta}t. \tag{26}$$

Considering only the evolution of domains at long times and applying the analysis described in the previous section, Eq. 26 reduces to

$$\frac{1}{9}a^3\left[3\ln\left(\frac{1}{2}\right)+3\epsilon+1\right] - \frac{1}{9}a_0^3\left[3\ln\left(\frac{L}{2a_0}\right)+1\right] = \frac{k_{\mathrm{B}}T\phi_{\mathrm{A}}}{16\eta}t \tag{27}$$

where $L/a = 1 + \epsilon$ such that $\epsilon \ll 1$ and $\ln\left(\frac{L}{2a}\right) = \ln(1/2) + \epsilon + \mathcal{O}(\epsilon^2)$. Thus domains grow approximately as

$$a = \left(kt + ba_0^3\right)^{1/3} \tag{28}$$

where $k = \frac{9k_{\mathrm{B}}T\phi_{\mathrm{A}}}{16\eta\left(3\ln\frac{1}{2}+3\epsilon+1\right)}$ and $b = 3\ln\left(\frac{L}{2a_0}\right)+1$.

Thus, domains that grow from $a_0 = 0$, purely by coalescence, follow the scaling

$$a \sim t^{1/3}. \tag{29}$$

2. Domain growth in simple shear flow

To evaluate the effect of flow on domain growth, we again solve the Smoluchowski equation (Eq. 13), but with convective flux due to an imposed shear flow, $\mathbf{U} = \dot{\gamma} r \mathbf{e_r}$, where $\dot{\gamma}$ is the shear rate:

$$\mathbf{j}_{\mathrm{rel}} = \mathbf{U}g - D_{\mathrm{c}}\left(\nabla_r g + g\frac{\nabla_r V}{k_{\mathrm{B}}T}\right). \tag{30}$$

In non-dimensional form, the Smoluchowski equation is

$$\frac{\partial g}{\partial t} + \mathrm{Pe_c}\nabla_r \cdot \mathbf{r}g - \nabla_r \cdot \left(\nabla_r g + g\frac{\nabla_r V}{k_{\mathrm{B}}T}\right) = 0. \tag{31}$$

The colloidal Péclet number is $\mathrm{Pe_c} = \dot{\gamma}a^2/D$, and is distinct from the Péclet number Pe used in the simulations, as its characteristic length scale a and diffusivity D correspond to whole domains, and are not molecular (lipid) parameters.

To solve Eq. 31, we assume that g can be expanded in powers of $\mathrm{Pe_c}$ as $g = n^2(g_0 + \mathrm{Pe_c}\, g_1 + \mathcal{O}(\mathrm{Pe_c}^2))$ in the limit $\mathrm{Pe_c} \ll 1$. The leading order term, g_0, is the solution for the passive case, with boundary conditions $g(r = 2a) = 0$ and $g(r = L) = n^2$.

$$g_0 = \frac{\ln(r/2a)}{\ln(L/2a)} \tag{32}$$

The steady-state behavior far away reveals that there is a boundary layer.

$$\nabla_r \cdot \underbrace{\left(\nabla_r g_0 + g_0 \frac{\nabla_r V}{k_\mathrm{B}T}\right)}_{\frac{1}{r}\sim 0} + \mathrm{Pe_c}\nabla_r \cdot \left(\nabla_r g_1 + g_0 \frac{\nabla_r V}{k_\mathrm{B}T}\right) = \mathrm{Pe_c}\nabla_r \underbrace{\cdot \mathbf{r} g_0}_{r\frac{\ln(r/2a)}{\ln(L/2a)}\sim\infty} + \mathcal{O}(\mathrm{Pe_c}^2) \tag{33}$$

As $r \to \infty$, convection dominates diffusion in the small $\mathrm{Pe_c}$ limit. By matching the order of both terms, we get $\mathrm{Pe_c}\, r^2 \ln(r/2a)/\ln(L/2a) \sim 1$. We argue that for large r and very small $\mathrm{Pe_c}$ such that $L/a \gg 1/\sqrt{\mathrm{Pe_c}}$, we can approximate the balance as $\mathrm{Pe_c}\, r^2 \sim 1$. Thus, the boundary layer region is re-scaled as $r \sim {\mathrm{Pe_c}}^{-1/2}$.

After performing a singular perturbation analysis at the boundary layer [9, 14, 15], and asymptotically matching with the solution at small r, we get an expression for the flux:

$$J = \frac{\pi k_\mathrm{B}T}{8\eta a \ln\left(\frac{L}{2a}\right)} n^2 \left(1 + C{\mathrm{Pe_c}}^{1/2}\right) \tag{34}$$

The constant C is a numerical factor obtained after asymptotic matching. Substituting this in Eq. 19, and assuming constant area fraction $\phi_\mathrm{A} = n\pi a^2$, as in the previous section gives

$$\frac{\mathrm{d}a}{\mathrm{d}t} = \frac{\pi k_\mathrm{B}T}{8\eta a^2 \ln\left(\frac{L}{2a}\right)} (1 + C{\mathrm{Pe_c}}^{1/2}). \tag{35}$$

We approximate the log to be constant, using the same argument as in the previous sections: at long times, when domain size is relatively large, $\ln \frac{L}{2a} = \ln(1/2) + \ln(1 + \epsilon) = \ln(1/2) + \epsilon + \mathcal{O}(\epsilon^2)$ where $\epsilon \ll 1$. Thus, we approximate Eq. 36 as

$$\frac{\mathrm{d}a}{\mathrm{d}t} \approx \frac{m}{a^2} (1 + C{\mathrm{Pe_c}}^{1/2}). \tag{36}$$

where $m = \frac{\pi k_\mathrm{B}T}{8\eta(\ln \frac{1}{2} + \epsilon)}$ is a constant.

The Péclet number depends on a as $\mathrm{Pe_c} = \dot{\gamma} a^2/D_\mathrm{c} = 16\dot{\gamma}\eta a^3/(k_\mathrm{B}T)$ for domains much larger than the Saffman-Delbrück limit (see previous section). The solution to Eq. 36 is

$$\frac{2}{3C_1^2}[C_1 a^{3/2} - \ln(1 + C_1 a^{3/2})] = C_0 + mt \ . \tag{37}$$

Here, $C_1 = C(16\dot{\gamma}\eta/(k_\mathrm{B}T))^{1/2}$, and $C_0 = (2/3C_1^2)(C_1 a_0^{3/2} - \ln(1 + C_1 a_0^{3/2}))$. Note that the term $C_1 a^{3/2}$ has no dimensions. When $C_1 a^{3/2} \ll 1$, we can expand $\ln(1 + C_1 a^{3/2})$ as a power series:

$$\frac{2}{3}\left[\frac{a^3}{2} + \mathcal{O}\left((C_1 a^{3/2})^3\right)\right] = C_0 + mt \implies a \sim t^{1/3} \ . \tag{38}$$

We see that passive growth dominates when $C_1 a^{3/2}$ is small. Similarly, when $C_1 a^{3/2}$ is large, we get

$$\frac{2}{3}\left[\frac{a^{3/2}}{C_1} - \frac{\ln(C_1 a^{3/2})}{C_1} + \mathcal{O}\left((C_1 a^{3/2})^{-1}\right)\right] = C_0 + mt \implies a \sim t^{2/3} \ . \tag{39}$$

The $a^{3/2}$ term dominates the log terms in the expansion, so effectively, the domain size scales as $t^{2/3}$ at long times.

3. Perturbation analysis for Cahn-Hilliard model with shear flow

The non-dimensional convective Cahn Hilliard equation is

$$\frac{\partial \phi}{\partial t} + \mathrm{Pe}\, \mathbf{v} \cdot \nabla \phi = \nabla^2(\phi^3 - \phi - \nabla^2 \phi) \ . \tag{40}$$

Here, the characteristic length and time scales are $\sqrt{\kappa}$ and κ/M respectively. We express shear velocity as $\mathbf{v} = \mathbf{G}\cdot\mathbf{x}$, where $\mathbf{G} = \left(\begin{smallmatrix} 0 & 1 \\ 0 & 0 \end{smallmatrix}\right)$. This gives us an analytic form of the Fourier-transformed convective term.

$$\mathcal{F}[\mathbf{v}\cdot\nabla\phi] = \mathcal{F}\left[G_{ij}x_j\frac{\partial\phi}{\partial x_i}\right] = -G_{ij}\left(\delta_{ij}\phi_k + k_j\frac{\partial\phi_k}{\partial k_i}\right) \tag{41}$$

We simplify further by linearizing the bulk free energy about the initial concentration ϕ_0 to give $\phi^3 - \phi \approx (3\phi_0^2 - 1)\phi - 2\phi_0^3$. Now, we have a linear equation in Fourier space.

$$\frac{\mathrm{d}\phi_k}{\mathrm{d}t} - \mathrm{Pe}\,G_{ij}\left(\delta_{ij}\phi_k + k_j\frac{\partial\phi_k}{\partial k_i}\right) = \left[(1-3\phi_0^2)k^2 - k^4\right]\phi_k \tag{42}$$

At small Pe limit, we expand ϕ_k in powers of Pe as $\phi_k = \phi_{k0} + \phi_{k1}\mathrm{Pe} + \mathcal{O}(\mathrm{Pe}^2)$. The leading order solution is

$$\phi_{k0}(t) = \phi_k(0)\exp\left[\left((1-3\phi_0^2)k^2 - k^4\right)t\right]\ . \tag{43}$$

Using the $\mathcal{O}(1)$ solution, we solve the $\mathcal{O}(\mathrm{Pe})$ differential equation to obtain ϕ_{k1}.

$$\phi_{k1}(t) = \mathrm{Pe}\,\phi_k(0)\exp\left[\left((1-3\phi_0^2)k^2 - k^4\right)t\right] \times k_x k_y((1-3\phi_0^2) - 2k^2)t^2 \tag{44}$$

The final expression for ϕ_k is

$$\frac{\phi_k(t)}{\phi_k(0)} = \exp\left[\left((1-3\phi_0^2)k^2 - k^4\right)t\right] \times \left[1 + \mathrm{Pe}\ k_x k_y\left((1-3\phi_0^2) - 2k^2\right)t^2\right] + \mathcal{O}(\mathrm{Pe}^2)\ . \tag{45}$$

We calculate domain size using the first moment of the static structure factor $S(k) = \langle\phi_k\phi_{-k}\rangle$, finding $a(t) \sim t^{1/4} + \mathrm{Pe}\,t^{5/4} + \mathcal{O}(\mathrm{Pe}^2)$.

IV. SIMULATION DETAILS

The Cahn-Hilliard model is solved numerically using pseudo-spectral methods. The evolution of the Fourier transformed order parameter ϕ_k is

$$\frac{\mathrm{d}\phi_k}{\mathrm{d}t} + \mathcal{F}[\mathbf{v}\cdot\nabla\phi] = -Mk^2\mathcal{F}\left[\frac{\delta f}{\delta\phi}\right] - M\kappa k^4\phi_k\ . \tag{46}$$

This first-order differential equation is solved using forward difference. The higher order gradient terms (∇^4) are treated implicitly. The bulk free energy, $\delta f/\delta\phi = \phi^3 - \phi$, and the convection term are non-linear so a 2/3 anti-alias filter is applied to remove high-frequency noise.

The initial system configuration is $\phi = \phi_{\mathrm{avg}} + 0.1\times(\text{white noise})$. For the main text figures, the average concentration is $\phi_{\mathrm{avg}} = 0.3$. The system is a 512^2 grid of length 32π. The time step is controlled with adaptive time stepping, $\Delta t_{new} = [\mathrm{tol}/(\phi(t;\Delta t) - \phi(t;\Delta t/2))]^{1/5}$. Here, $\phi(t;\Delta t)$ means using a time step Δt to calculate $\phi(t)$, and the tolerance, tol is 10^{-4}.

A. Metric for domain size

In the main text, the domain size is calculated using area/perimeter. There is an alternate metric based on the structure factor of domains, $S(k,t) = \langle\phi_k(t)\phi_{-k}(t)\rangle$, that also yields similar results. In this metric, the domain size is the inverse of the first moment of the structure factor:

$$a(t) = \frac{\int_{k_{\mathrm{min}}}^{k_{\mathrm{cut}}} S(k,t)\mathrm{d}k}{\int_{k_{\mathrm{min}}}^{k_{\mathrm{cut}}} kS(k,t)\mathrm{d}k}. \tag{47}$$

Here k_{min} is the minimum non-zero wave-number, $k_{\mathrm{cut}} = 2k_{\mathrm{max}}$ is the cut-off wavelength, and k_{max} is the wave number corresponding to the maximum value of the structure factor. Fig. S5 shows that using the area/perimeter ratio of domains yields similar scaling for $a(t)$ as the first moment of the static structure factor.

V. SUPPLEMENTAL FIGURES

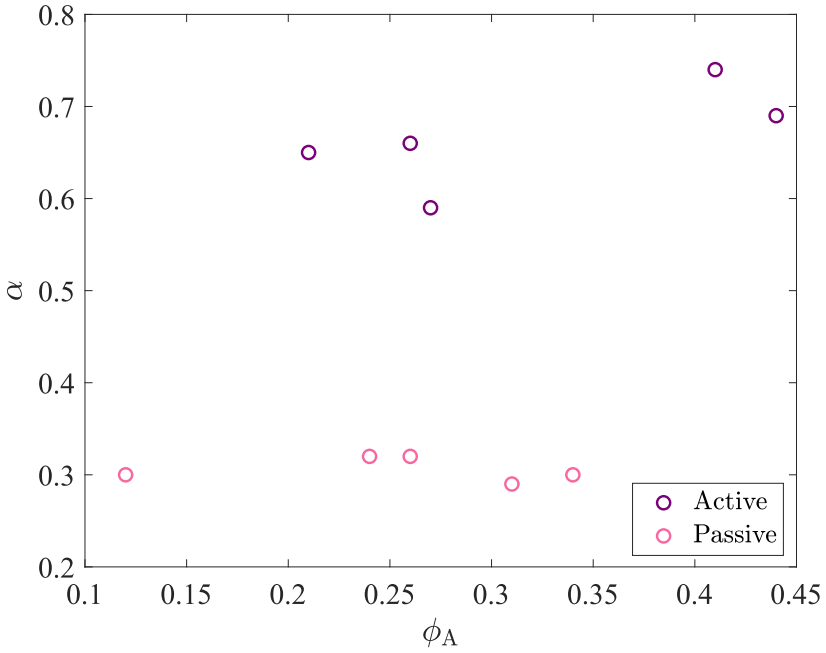

FIG. S1. The growth exponent of lipid domains α, defined according to the relation between domain size a and time t, $a \sim t^{\alpha}$, is plotted as a function of domain area fraction ϕ_A for both passive and active experiments. As passive systems were heated and quenched to determine the growth rate, the passive area fractions presented are measured at the end of each quench. For active systems, the area fractions are measured at the beginning of each image sequence, but are approximately constant as the experimental system remains at room temperature. For both systems, there is little apparent correlation between area fraction and growth rate. All lipid vesicles are prepared using 45% DOPC, 35% DPPC, 15% cholesterol, and 5% DOTAP, except for the active experiment at $\phi_A = 0.21$, for which the composition was 52% DOPC, 25% DPPC, 15% cholesterol, and 8% DOTAP.

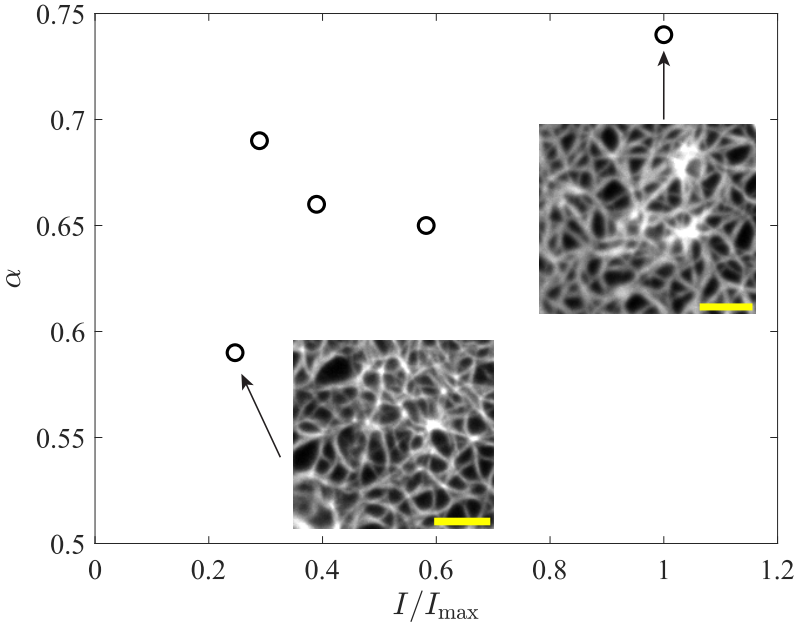

FIG. S2. Domain growth exponents α are plotted as a function of mean actin fluorescence intensities I, normalized by the fluorescence intensity of the brightest sample $I_{\max}$, for each actin-driven coalescence data set presented in Fig. 2. There may be a correlation between actin density and growth rate of lipid domains. Images of actin at the moment ATP was introduced are included for the samples with the lowest and highest actin densities. Scale bars are 5 µm.

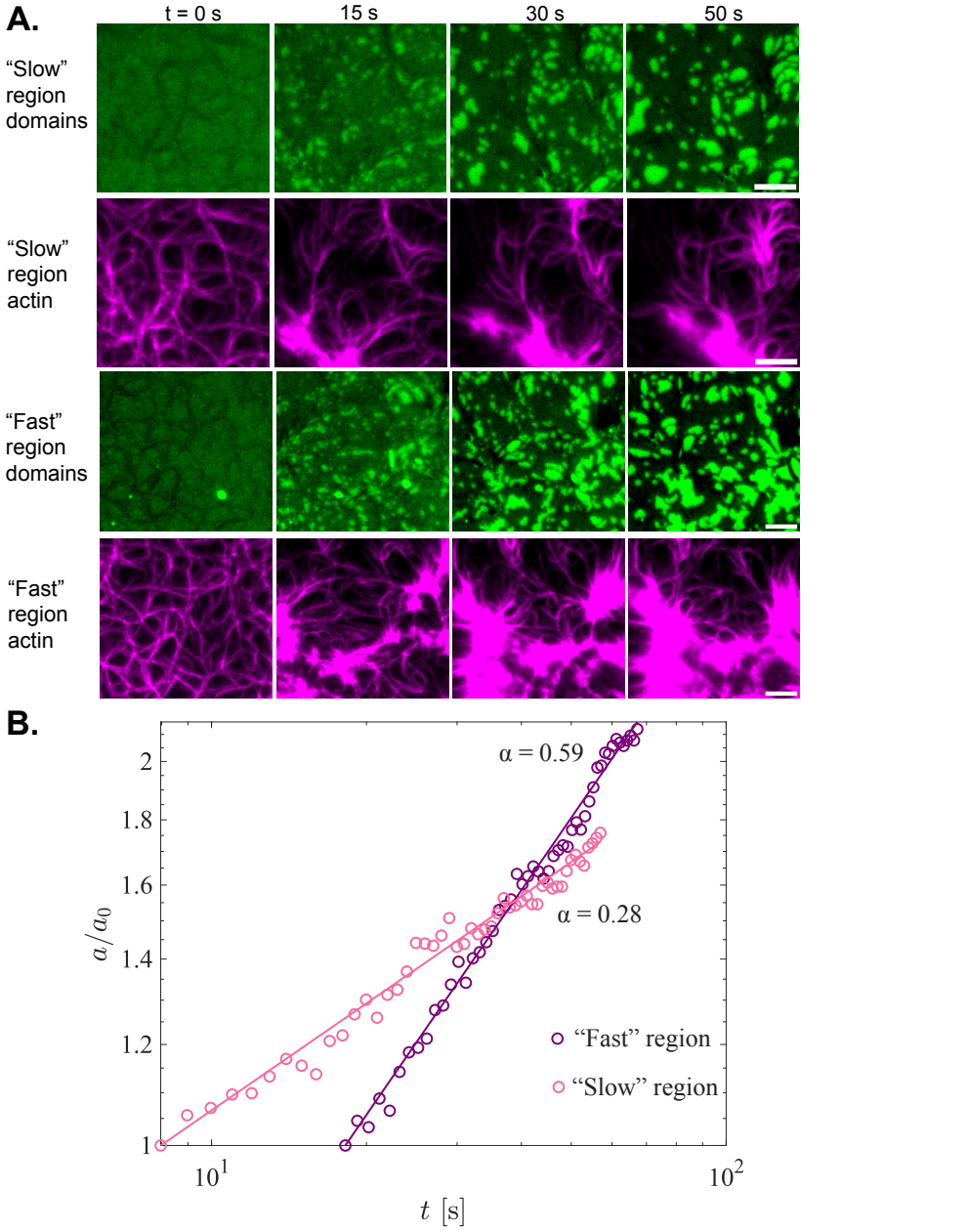

FIG. S3. Timing of actin-lipid interaction during bilayer quench dictates domain growth rate. (A) An actin-coated lipid bilayer is heated until the domains melt, and then cooled to room temperature. ATP is introduced at $t = 0$, approximately the same time at which domains began to nucleate and coarsen. Two neighboring, and partially overlapping, regions of interest are sampled, and the domain growth analyzed. In the "slow" region (top two rows), actin is rapidly pulled into contractile centers at the periphery of the image, with the most widespread activity qualitatively occurring between 0 and 15 s (second row, magenta). Domains becomes resolvable at approximately 15 s (top row), after the most widespread activity has passed. In contrast, in the "fast" region (bottom two rows), actin contracts toward the center of the images, sustaining widespread flows throughout domain coarsening. Scale bars are 5 µm. (B) Domain growth is plotted as a function of time for both "fast" and "slow" regions of the sample. The "slow" region approximates passive growth, wherein domain size a increases with time t as $a \sim t^{\alpha}$ where $\alpha = 0.28 \approx 1/3$. In the "fast" region, sustained actin flows drive enhanced scaling $\alpha = 0.59$. The time axis for each data set is re-scaled by fitting data to an equation of the form $a = (At + B)^{\alpha}$ with the plotted time related to the timescale of experiment by $t_{\mathrm{plot}} = t_{\mathrm{absolute}} + B/A$. Domain size a is re-scaled by initial domain size measured for each data set, a_0.

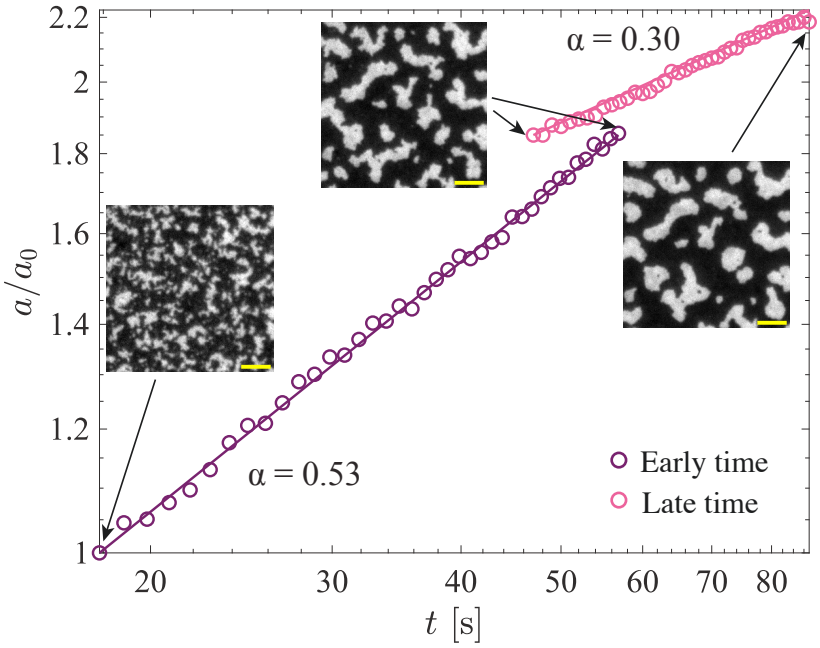

FIG. S4. Near-critical lipid bilayers phase-separate according to a spinodal decomposition mechanism. Domain size a, normalized by the initial domain size a_0 is plotted as a function of time t for a near-critical lipid bilayer undergoing passive growth after a quench. Domain size was recorded for the first 40 seconds of an experiment (early time) and again for the following 40 seconds (late time). The time axis for each data set is re-scaled by fitting data to an equation of the form $a = (At + B)^{\alpha}$ with the plotted time related to the timescale of experiment by $t_{\text{plot}} = t_{\text{absolute}} + B/A$. Thus the endpoint for the early time and starting point for late time datasets are the same. Representative images are shown, with scale bars of 5 µm. At early times, domains grow according to a^{α} with $\alpha \approx 1/2$, before returning to $\alpha \approx 1/3$ at later times, consistent with prior measurements on lipid bilayers by Stanich et al. [13]. Our active flows are always introduced at late times, and we thus compare active experiments to the late-time behavior for these near-critical passive experiments.

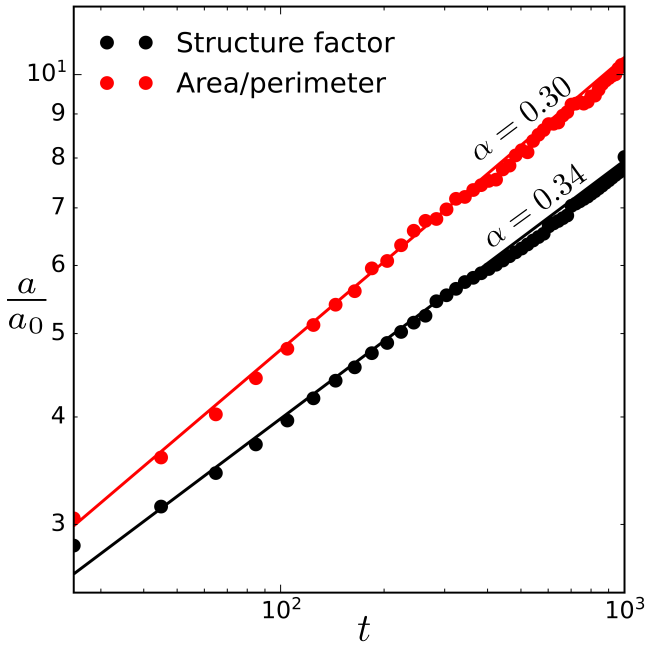

FIG. S5. Comparison of area/perimeter and structure factor as metrics for domain size for passive coarsening. Domain growth scales similarly regardless of the metric used to quantify domain size. The simulation parameters are (M, κ)=(1, 0.25).

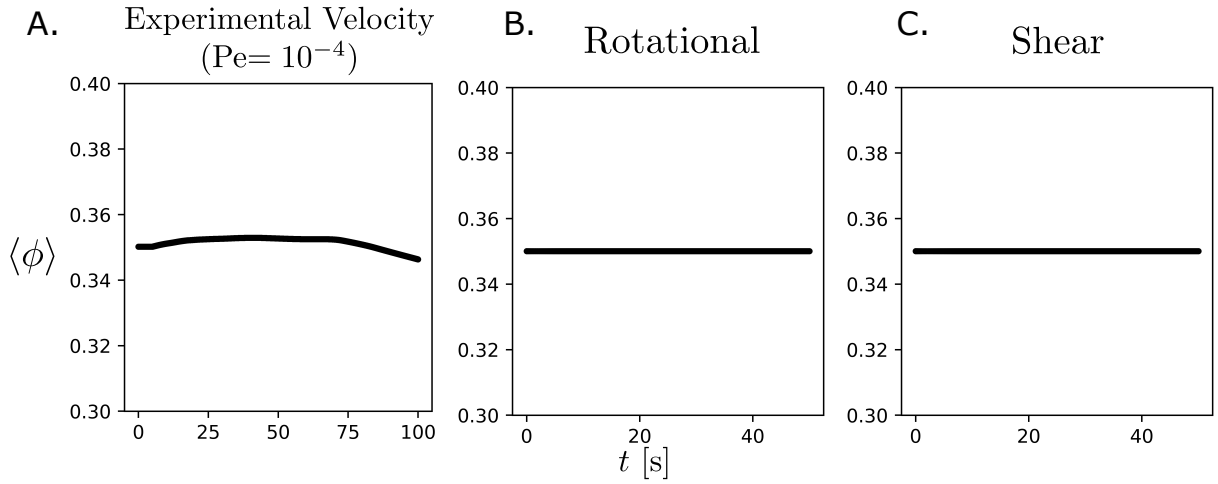

FIG. S6. "Mass", $\langle\phi\rangle(t) = \int \mathrm{d}\mathbf{x}\, \phi(\mathbf{x}, t)$ of the simulated phase field is plotted as a function of time t for (A) the flow field derived from experiment with Pe=10^{-4}, (B) rotational flow, and (C) shear flow. In simulations with flow, the mass is exactly constant. In the experimental flow profile, the mass is approximately constant over the fitted range of time.

[1] J. A. Spudich and S. Watt, The Regulation of Rabbit Skeletal Muscle Contraction, Journal of Biological Chemistry **246**, 4866 (1971).

[2] S. MacLean-Fletcher and T. D. Pollard, Identification of a factor in conventional muscle actin preparations which inhibits actin filament self-association, Biochemical and Biophysical Research Communications **96**, 18 (1980).

[3] S. S. Margossian and S. Lowey, Preparation of myosin and its subfragments from rabbit skeletal muscle, in *Methods in Enzymology*, Vol. 85 (Elsevier, 1982) pp. 55–71.

[4] M. I. Angelova and D. S. Dimitrov, Liposome electroformation, Faraday Discussions of the Chemical Society **81**, 303 (1986).

[5] C. F. E. Schroer, L. Baldauf, L. van Buren, T. A. Wassenaar, M. N. Melo, G. H. Koenderink, and S. J. Marrink, Charge-dependent interactions of monomeric and filamentous actin with lipid bilayers, Proceedings of the National Academy of Sciences **117**, 5861 (2020).

[6] A. D. Edelstein, M. A. Tsuchida, N. Amodaj, H. Pinkard, R. D. Vale, and N. Stuurman, Advanced methods of microscope control using μManager software, Journal of Biological Methods **1**, e10 (2014).

[7] I. Lifshitz and V. Slyozov, The kinetics of precipitation from supersaturated solid solutions, Journal of Physics and Chemistry of Solids **19**, 35 (1961).

[8] A. J. Bray and C. L. Emmott, Lifshitz-Slyozov Scaling For Late-Stage Coarsening With An Order-Parameter-Dependent Mobility, Phys. Rev. B **52**, R685 (1995).

[9] W. B. Russel, D. A. Saville, and W. R. Schowalter, *Colloidal Dispersions* (Cambridge University Press, 1989).

[10] E. D. Siggia, Late stages of spinodal decomposition in binary mixtures, Physical Review A **20**, 595 (1979).

[11] V. Frolov, Y. Chizmadzhev, F. Cohen, and J. Zimmerberg, "Entropic Traps" in the Kinetics of Phase Separation in Multicomponent Membranes Stabilize Nanodomains, Biophysical Journal **91**, 189 (2006).

[12] N. Oppenheimer and H. A. Stone, Effect of Hydrodynamic Interactions on Reaction Rates in Membranes, Biophysical Journal **113**, 440 (2017).

[13] C. A. Stanich, A. R. Honerkamp-Smith, G. G. Putzel, C. S. Warth, A. K. Lamprecht, P. Mandal, E. Mann, T. A. D. Hua, and S. L. Keller, Coarsening dynamics of domains in lipid membranes, Biophysical Journal **105**, 444 (2013).

[14] L. G. Leal, *Advanced Transport Phenomena* (Cambridge University Press, Cambridge, 2007).

[15] W. M. Deen, *Introduction to Chemical Engineering Fluid Mechanics*, Cambridge Series in Chemical Engineering (Cambridge University Press, 2016).